Measurement 182 (2021) 109738

Contents lists available at ScienceDirect

Measurement

journal homepage: www.elsevier.com/locate/measurement

Novel nano-scale absolute linear displacement measurement based on grating projection imaging

Hai Yu *, Qiuhua Wan, Zhiya Mu, Yingcai Du, Lihui Liang

Changchun Institute of Optics, Fine Mechanics and Physics, Chinese Academy of Sciences, Changchun 130033, People's Republic of China

ARTICLE INFO

Keywords:
Image-type displacement measurement
High resolution
High precision
Grating projection imaging

ABSTRACT

There is urgent demand for new absolute Linear Displacement Measurement (LDM) technology with high resolution and high precision, during the development of high-end numerical control technology. In previous research, we found that displacement measurement based on the image processing method performs well, however, the volume increases when using an imaging lens, and the system is susceptible to factors such as virtual focus. In this paper, the lensless LDM image optical path is established based on grating projection imaging, then the absolute grating coding method is operated based on $M-$sequence pseudo-random coding. A linear displacement subdivision algorithm is then deployed based on the digital image recognition algorithm. An LDM device with a measuring range of 250 *mm* was designed to test the performance of the proposed method. The device shows a measurement resolution of 1 *nm* and measurement accuracy of 1.76 μ*m* in the range of 250 *mm*. This work lays a foundation for further research on high performance LDM technology.

1. Introduction

Existing techniques for high-precision digital Linear Displacement Measurement (LDM) mainly include photoelectric measurement, magnetic induction measurement, and capacitance measurement [1–4]. Among them, photoelectric LDM technology integrates optical, mechanical, and electrical qualities; it features high measurement accuracy, wide measurement range, strong anti-interference, and other advantages making it a preferred approach in industrial manufacturing, aerospace, military equipment, and other fields [5–7]. As a feedback method in the control system, improvements in the resolution, accuracy, and reliability of photoelectric displacement measurement are directly related to the high-end manufacturing capacity available. There is demand for new absolute photoelectric displacement measurement technology with high resolution and high precision to meet the needs for high-performance numerical control system in today's high-end manufacturing industry.

Traditional photoelectric displacement measurement technology generates a moiré fringe signal based on the mutual cooperation of an indication grating and calibration grating, and then realizes high-resolution displacement measurement by calculating the phase of the moiré fringe signal [8]. Its measurement principle is shown in Fig. 1.

During the measurement process, reference lines with equal period are scratched on the calibration grating. The light emitted by the light-emitting element passes through the grating line on the calibration grating, then two moiré fringes with phase difference of 1/4 period are generated by the cooperation of the indicating grating. The moiré fringe light signal is converted into an electrical signal by the photosensitive element. The relative displacement of the calibration grating and the indication grating can be calculated by "subdivision operation" of the electrical signal phase. For the purposes of absolute measurement, traditional measurement technology requires marking coding lines on the calibration grating for absolute position recognition, then realizing decoding via the recognition of the coding lines. The absolute displacement measurement is obtained by combining the decoded value and the subdivision value.

Through previous studies, the shortcomings of the traditional absolute photoelectric LDM technology can be summarized as follows.

1) Performance is not readily improved

The Moiré fringe signal is easily affected by harmonic noise, amplitude difference, phase difference offset, and other factors; it is difficult to further improve the measurement accuracy and resolution.

2) Debugging is overly complex

* Corresponding author.
E-mail address: yuhai@ciomp.ac.cn (H. Yu).

https://doi.org/10.1016/j.measurement.2021.109738
Received 19 April 2021; Received in revised form 6 June 2021; Accepted 7 June 2021
Available online 22 June 2021

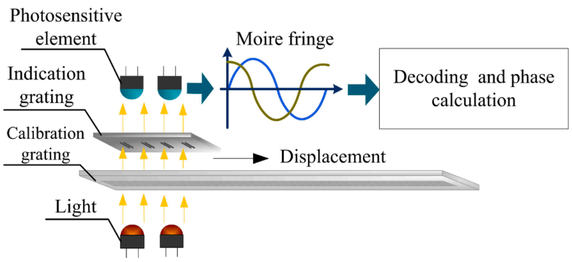

Fig. 1. Moiré fringe measurement principle.

Absolute photoelectric measurement methods require "coding codes" and "subdivision values" to cooperate with each other. Ensuring such cooperation is a cumbersome process of steps such as "phase alignment" and "period correction" during installation, which needs repeated debugging to ensure the measurement accuracy.

There is demand for new displacement measurement methods to remedy these problems. Image-type displacement measurement is an innovative approach based on the digital image processing algorithm [9–12]. This method can achieve high-performance LDM. When a camera is used to collect the pattern on the calibration grating, the LDM can be realized via digital image processing algorithm [13]. This measurement principle is shown in Fig. 2.

In a previous study, we developed angular displacement measurement (ADM) technology based on an image processing algorithm [14,15]. We found that image-type displacement measurement has strong flexibility, robustness, and fault tolerance; it is not affected by the amplitude difference, phase offset, period correction, or other factors of the traditional Moiré fringe measurement technology. We speculated that applying image-type measurement to LDM would have the following advantages.

1) Strong fault tolerance

There is no tedious debugging process required for absolute measurement based on the recognition of grating image information.

2) High performance

High accuracy and high resolution can be more easily achieved than traditional measurement methods based on the sub-pixel algorithm.

Previous scholars have explored LDM technology based on image processing algorithms as well. Das [16], for example, proposed an LDM method based on gray gradients in 2013 which can realize measurement resolution of 1 *mm*. Baji [17] proposed an LDM method based on color recognition in 2014 that can measure the rotation angle of a code disk coated with uniform color change at a linear error of 1°. Existing measurement methods based on color recognition can achieve absolute measurement, but the measurement resolution is limited.

In a 2015 study, Kim [18] used the phase-shifting encoding method with a micro image detection system to realize 13-bit encoding recognition on a 41.72 *mm* diameter grating at measurement accuracy of 0.044°. Mu [19] used a CMOS image sensor to recognize single code channel coding for 20-bit coding recognition. Due to a lack of subdivision operation, however, the displacement measurement resolution is relatively low and the technique is restricted to coding recognition.

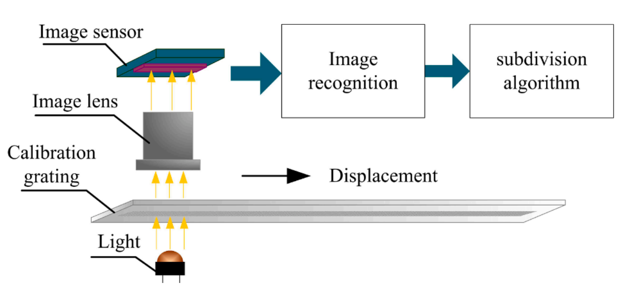

Fig. 2. Schematic diagram of image-type LDM.

Leviton [20] received grating patterns with reference lines and binary symbols with an area array CCD, then magnified the image with an optical lens to achieve a measurement resolution of 0.05 μ*m* and precision of 0.15 μ*m* in the range of 150 *mm*. Lashmanov [21] used a camera to collect and measure the linear displacement with scale lines, achieving a resolution of 0.02 μ*m* and a measurement accuracy of 1.65 μ*m* in the range of 2 *m*. Fu [22] proposed a image grating technique is presented achieve ± 0.3 μ*m* measurement accuracy within a 50 mm range and ± 0.2 μ*m* measurement accuracy within a 25 mm range. It is relatively easy to enhance measurement resolution by using an imaging lens to magnify the image, but this makes the measurement device larger, the optical path more complex, and the system more vulnerable to vibration, virtual focus, and other effects.

In this study, we developed a high-resolution LDM method which does not require an imaging lens and work based on grating projection imaging. The lensless measurement light path based on grating projection imaging was established first. An absolute coding method based on $M-$sequence pseudo-random code was then established. Finally, a subpixel subdivision algorithm was constructed to achieve high-resolution measurement. An experimental device was designed and operated to test the proposed method. The range of the experimental device is 250 *mm* when 500 coded lines are marked in the range. This LDM device shows a measurement resolution of 1 *nm* and measurement accuracy of 1.78 μ*m*. This work may provide a workable foundation for future high-resolution, high-reliability LDM technologies.

This paper is organized as follows. Section 2 introduces the principle of the image-type LDM optical path. Section 3 proposes the absolute encoding method and discusses its identification process. Section 4 proposes the linear displacement subdivision algorithm. Section 5 presents the experimental verification and Section 6 gives a brief summary and concluding remarks.

2. Measurement optical path of grating projection imaging

Using an imaging lens to magnify an image can improve the measurement resolution, but as discussed above, makes the measurement device larger, the optical path more complex, and the system more vulnerable to vibration, virtual focus, and other effects. We propose an

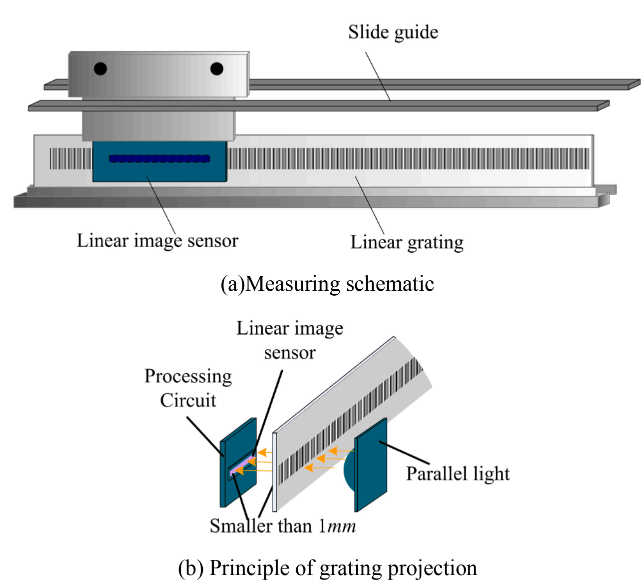

Fig. 3. (a) Measuring schematic Fig. 3 (b) Principle of grating projection.

LDM optical path based on grating projection imaging which works on the principle shown in Fig. 3.

During the measurement process, the light emitted by the parallel light source passes through the “leaky” coding lines on the metal grating. The pattern of the coding lines is projected on the linear image sensor. LDM can then be realized by the sub-pixel subdivision algorithm.

To minimize the effects of light wave diffraction and improve the sub-pixel subdivision ability, we attempted to reduce the distance between the linear image sensor and the linear grating to no more than 1 *mm*. As the linear scan image sensor moves along the measurement direction, it collects the projection pattern of the coded line on the linear grating and then realizes the decoding, subdivision, and other operations.

3. Absolute coding and identification

3.1. Absolute encoding

The traditional grating marking method involves marking “grating lines” with equal period, equal spacing, and equal width in the linear range. Here, we transformed the grating lines into “wide” and “narrow” to form a “wide” coded line and “narrow” coded line to secure absolute grid line position values, which respectively represent “1” and “0” coding elements.

If the linear grating contains M coding intervals, then at least $M + m$-1 coded lines are needed (the binary digits of M are m). When we identify $M + m$-1 codes, we must obtain the binary code value of m-bit. If the coding element represented by the i-th coded line is X_i, we set m-bit coded value are $\{X_i, X_{i+1}, \dots, X_{i+9}, X_{i+m-1}\}$, and the adjacent m coding elements form a group of codes that are expressed as $\{X_i, X_{i+1}, \dots, X_{i+9}, X_{i+m-1}\}$. As the linear image sensor moves along the grating direction, the recognized coding group changes from $\{X_i, X_{i+1}, \dots, X_{i+m-2}, X_{i+m-1}\}$ to $\{X_{i+1}, X_{i+2}, \dots, X_{i+m-1}, X_{i+m}\}$ and form a new coding group (Fig. 4).

Moving the image sensor M times produces M group coding. We set the initial coding group as {0,0,0,0,0,0,0,0,0,1} (#1 coding group in Fig. 4). We calculated the value of each bit code-element X_i by “XOR” operation of the first m coding element values to ensure that each coding group was unique:

$$X_i = k_1X_{i-1} \oplus k_2X_{i-2} \oplus \cdots \oplus k_mX_{i-m} \tag{1}$$

where“$\oplus$“represents the “XOR” operation and k_1-k_m is the coefficient (value “0” or “1”). Reasonable selection of the k_1-k_m value can produce up to 2^m groups of different codes with the previous M encoding group. We set the decoding value of each group of codes is A, which can be expressed as the value of i.

We set $M = 500$ here with the binary digits of M as $m = 9$-*bit*. We plugged the k_1-k_m values into MATLAB software. When it can produce up to 2^m groups of different codes, the code-element is confirmed as follows:

$$X_i = X_{i-1} \oplus X_{i-6} \tag{2}$$

No imaging lens is used in this case, so it is necessary to match the imaging range with the coding recognition region. We set the range of linear grating to L and the field length of linear scan image sensor is l_{sensor}. When the number of codes on the grating is M, the vision field of image sensor should contain at least m coded lines (the binary digits of M is m), that is, the value of M should meet the following constraint:

$$l_{sensor} \geqslant \frac{L}{M} \cdot m \tag{3}$$

3.2. Code recognition

When we recognized and decoded the encoded lines on the grating, we only needed to judge the “width” and “narrowness” of each line in the imaging field l_{sensor} to obtain the encoded value. The decoding value of the current position can be obtained by looking it up in the decoding table. The code recognition principle is shown in Fig. 5.

According to Fig. 5, when the number of coded lines is $m = 9$-bit, the image collected by the image sensor contains 9 coded lines. To determine their respective widths, we binarized the image and calculated the value W_j of the j-th coded line accordingly. Because the distance between adjacent coding lines is L/M, we set the width threshold $\beta = L/2M$ and calculated the value expressed by the coding element C_j as follows:

$$C_j = \begin{cases} 1, W_j \geqslant \beta \\ 0, W_j < \beta \end{cases} \left(j = 1, \dots, 9\right) \tag{4}$$

Equation (4) reveals the C_j value of j = 1–9. As shown in Fig. 5, the recognized coding group was $\{C_1, C_2, \dots, C_9\}$={0, 1, 0, 0, 1, 1, 1, 1, 1}. We can get the decoding value to A ($A = i$) according to the decoding lookup table.

4. Subdivision algorithm

4.1. Location algorithm

Subdivision is realized by locating the coded lines accurately. We adopted the coding line positioning algorithm based on quadratic function fitting algorithm [13] for enhanced robustness, as shown in Fig. 6.

In Fig. 6, x is the pixel positions, $y(x)$ is the gray value of x-th pixel. The gray value curve of the coding line approximates a quadratic function curve. We used the following quadratic function to fit it:

$$f(x) = c_1x^2 + c_2x + c_3 \tag{5}$$

where c_1, c_2, and c_3 are the coefficients. We minimized the square of the difference between $f(x)$ and $y(x)$ to determine the coefficients:

$$F = min\{\sum [f(x) - y(x)]^2\} \tag{6}$$

We can represent the location of the coding line by the maximum value of the function $f(x)$. The positioning values can be calculated as follows:

$$x_k = -\frac{c_2}{2c_1} \tag{7}$$

where x_k represents the position of the k-th coding line in the image.

We used multiple acquisition to de-noise the positioning operation result. If the positioning value of the k-th line is $x_k(i)$ at time i, then the

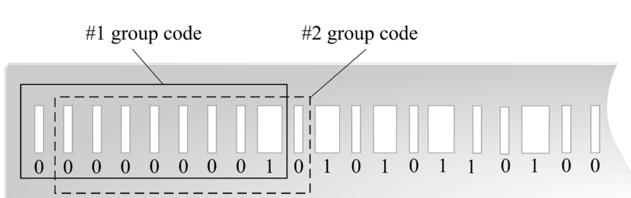

Fig. 4. Coding principle ($m = 9$).

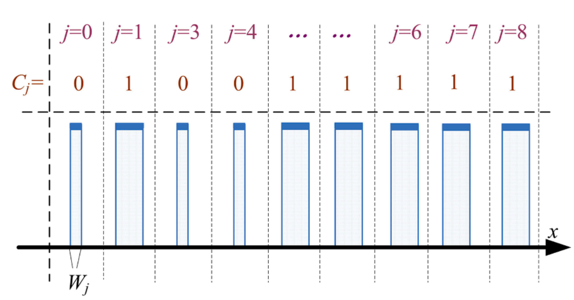

Fig. 5. Coding recognition principle.

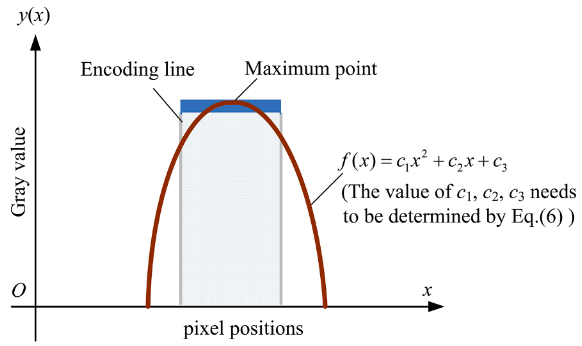

Fig. 6. Quadratic fitting location algorithm.

values of the previous n acquisition are $x_k(i\text{-}1)$, $x_k(i\text{-}2)$,…, $x_k(i\text{-}n\text{-}1)$,…,$x_k(i\text{-}n)$, respectively. The mean value between the values at time i and the previous n times can be calculated to obtain a stable positioning value:

$$x_k'(i)=\frac{x_k(i)+x_k(i-1)+x_k(i-2)+\ldots+x_k(i-n)}{n+1} \tag{8}$$

Equation (8) is an $n+1$ order de-noising algorithm that can effectively suppress noise because it takes the average value among all values at adjacent sampling times.

Finally, we used the de-noised x'_k for subdivision operation.

4.2. Subdivision algorithm

According to the LDM principle, a lack of uniformity in the coded lines on the linear grating affects the measurement accuracy. To eliminate error, we fused multiple coded lines on the linear grating to calculate the subdivision interval. The linear array image information we collected is shown in Fig. 7.

In Fig. 7, x is the pixel positions, $y(x)$ is the gray value of x-th pixel. As shown in Fig. 7(a), we established a coordinate system with the center point of the image sensor as the zero point; the × axis of the coordinate system is the pixel position in the image and the y axis is the gray value of the pixel. The variables a_1-a_9 are the respective coding lines in the image. The lines with a_4 as the center symmetry are {a_1, a_7}, {a_2, a_6}, {a_3, a_5}; the symmetrical lines are centered on a_5 are {a_2, a_8}, {a_3, a_7}, {a_4, a_6}. We applied Equation (8) to calculate the position of all coded lines a_1-a_9, which are expressed as x'_1-x'_9, respectively. A multi-line fusion algorithm can then be applied to the end points of the subdivision interval on both sides of the image midpoint:

$$x_a=\frac{(x_1'+x_7')+(x_2'+x_6')+(x_3'+x_5')+x_4'}{7} \tag{9}$$

$$x_b=\frac{(x_2'+x_8')+(x_3'+x_7')+(x_4'+x_6')+x_5'}{7} \tag{10}$$

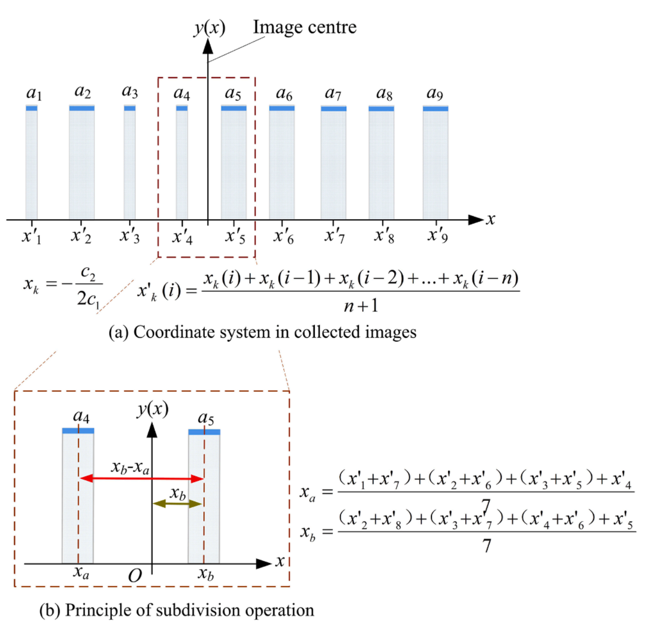

Fig. 7. (a) Coordinate system in collected images Fig. 7 (b) Principle of subdivision operation.

We next used the ratio algorithm for subdivision operation, as shown in Fig. 7(b); x_a and x_b are the end points of subdivision interval calculated by Equations (9) and (10), x_b-x_a is the length of the subdivision interval, and the distance between x_b and y axis is the subdivision offset. As per the relationship shown in Fig. 7(b),

In the subdivision operation, we assume that we expect to achieve η-fold subdivision operation. Then, it is necessary to realize the subdivision of a within the space range of coding lines (expressed as x_b-x_a). To realize the subdivision operation, we map x_b-x_a to the value of η. Therefore, the proposed subdivision operation is shown as follow:

$$B=\eta\cdot\frac{x_b}{x_b-x_a}=500000\cdot\frac{x_b}{x_b-x_a} \tag{11}$$

where η is the mapping value of the subdivision operation. Its physical meaning is the quantized value of the code line interval. A larger quantized η values indicates a higher achievable subdivision multiple. In this paper, we make $\eta=500000$.

After connecting the decoding value A and subdivision value B, the displacement measurement value D can be obtained alongside high-resolution measurement values. D can be expressed as follows:

$$D=A\cdot\eta+B \tag{12}$$

5. Experiment

To validate the proposed LDM method, we designed a linear grating with a length of 250 *mm* and built a sliding support for experimentation. The experimental device is shown in Fig. 8.

In order to improve the stain resistance of grating, we use metal materials to design and manufacture grating. Thus, a plurality of hollowed out coding lines are carved on the metal ruler. Although the design accuracy of metal grating is not as high as that of glass, the proposed method is verified in this experiment.

We use linear image sensor for measurement. There are [1 × 512] pixels in the image sensor with pixel size of 12.7 μ*m*. The field of vision of the image sensor is 6.5 mm. The measurement frequency response based on image sensor is 800 Hz.

The range of the designed linear grating is 250 *mm*. There are 500 coded lines in the range. The spacing of the coded lines is 250 *mm*/500 = 0.5 *mm*. We set $\eta=500000$ and achieved a 500000-fold subdivision by

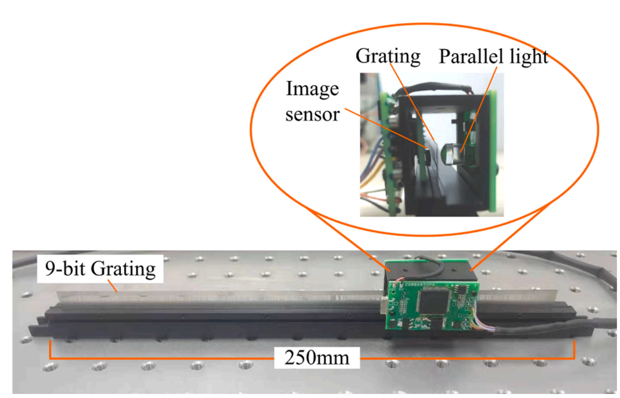

Fig. 8. Experimental device.

the subdivision algorithm, thus achieving a measurement resolution of 0.5 $mm/500000 = 1$ nm. All the key information is shown in Table1.

5.1. Measurement optical path verification

When 500 coded lines are scribed in the range of 250 mm, the number of coding recognition bits is 9-bit. Therefore, the image sensor needs to collect at least nine coded line patterns. The image collected by the linear image sensor is shown in Fig. 9(a), and the image after the [1 × 7] mean filtering algorithm is shown in Fig. 9(b). There are more than nine coded lines in the collected image; noise was eliminated after operating the mean filtering algorithm. The image contains a pattern of "wide and narrow" coded lines that can be used for LDM.

5.2. Decode verification

The image recognition algorithm was used to recognize the "wide" and "narrow" coded lines in the image. Then, we arrange all the coding arrays obtained by Equation (8) in order, and set the decoding value of one-to-one correspondence to $A = i$ ($i = 0 \sim 511$). Then the decoding table was queried to realize the decoding. When the image sensor moves slowly, the continuous acquisition codes are as shown in Table 2.

By moving image sensor, we found that decoding values were carried out successively and continuously when the image sensor moved continuously.

5.3. Location algorithm test

We verified the proposed location algorithm by first applying Equation (7) to continuously locate the a_6 line in Fig. 9(b), and collected 1000 positioning values. The fluctuation curve of the a_6 line positioning value is shown in Fig. 10(a); its fluctuation mean square error is 0.0013pixels.

Next, we used the multi-line fusion algorithm (Equation (10)) to locate the a_6 line. The result after 1000 consecutive acquisitions is shown in Fig. 10(b), where the mean square deviation of fluctuation is 0.0008879pixels.

Finally, we set $n + 1 = 9$ in Equation (8) to de-noise the a_6 line. The positioning result is shown in Fig. 10(c); its fluctuation mean square error is 0.00007489pixels.

The values appear to fluctuate in Fig. 10(a), but there is no such positioning noise shown in Fig. 10(c). Since the pixel spacing of the image sensor we used is 12.7 μm, so the measurement fluctuation caused by the noise is 12.7 μm × 0.00007489$pixel$≈0.00095 μm.The fluctuation value is less than 1 nm, which suggests that the proposed algorithm is effective.

5.4. Resolution test

We set η = 500000 and applied the proposed subdivision algorithm to the experimental device. Output values were gathered continuously 100 times as the experimental device was moved slowly, as shown in Fig. 11(a). The LDM output value jumped between 122923453 nm and 122923458 nm, with a single jump within 1 nm. There was no cross-resolution jump and the output was continuous in this case.

Table 1
Key information of experimental device.

Key specifications	Information
Resolution of linear image sensor	1 × 512pixels
Pixel size	12.7 μm
Imaging field of vision	6.5 mm
Measuring frequency response	800 Hz
Measuring range	250 mm
Measurement resolution	0.001 μm

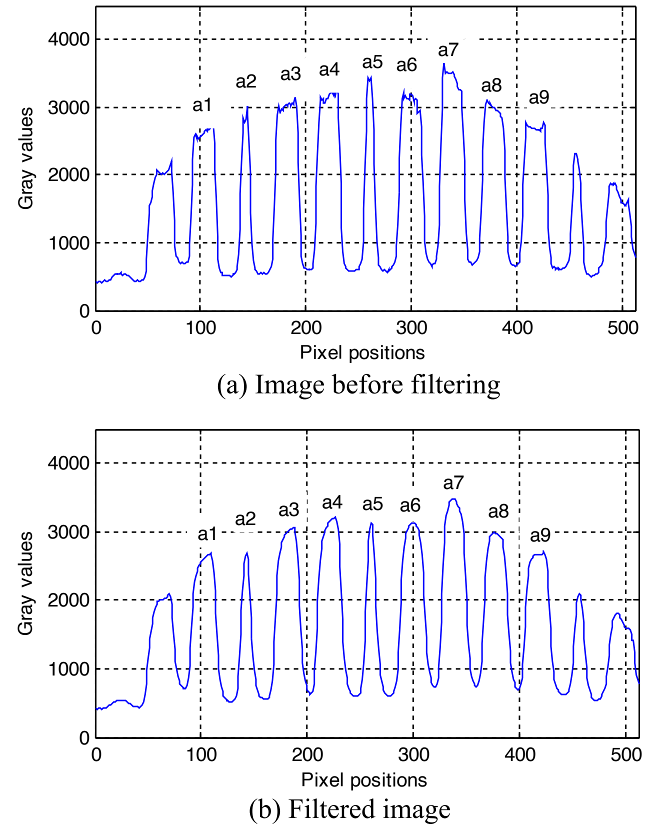

Fig. 9. (a) Image before filtering Fig. 9 (b) Filtered image.

Table 2
Decoding table.

NO.	Coded values	Decoding values
0	000,000,000	00,000,000
1	000,000,001	00,000,001
…	…	…
80	010,011,111	001,010,000
81	100,111,111	001,010,001
82	001,111,110	001,010,010
83	011,111,101	001,010,011
84	111,111,011	001,010,100
85	111,110,110	001,010,101
86	111,101,100	001,010,110
87	111,011,001	001,010,111
88	110,110,010	001,011,000
89	101,100,100	001,011,001
…	…	…
510	010,000,000	111,111,110
511	100,000,000	111,111,111

Next, we faster moved the image sensor and collected LDM output data 1000 times. As shown in Fig. 11(b), the LDM output values were accurate and continuously increased as the image sensor moved.

It can be seen that there is no error in the output of the proposed device. It achieved a measurement resolution of 1 nm.

5.5. Repeatability test

We used a laser interferometer to calibrate its error as shown in Fig. 12. The measurement temperature is room temperature(25℃).

In Fig. 12, the resolution of the laser interferometer is 1 nm and the linear measurement accuracy is 0.5 ppm, dynamic frequency is 50 kHz.

Five times measurements were carried out to verify the repeatability of the proposed equipment. Based on the laser interferometer, we record

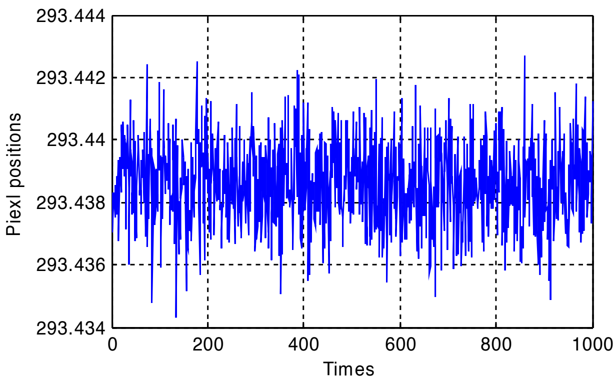

(a) Positioning wave curve

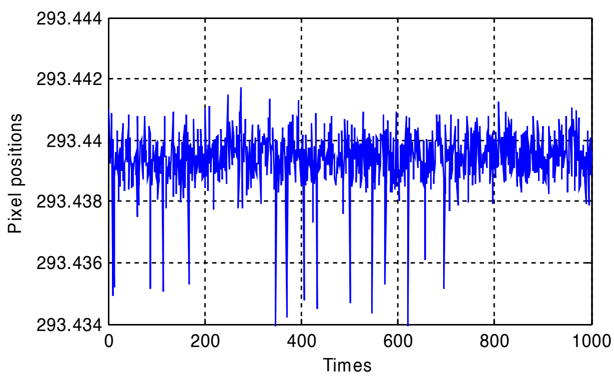

(b) Location result of multi-line fusion

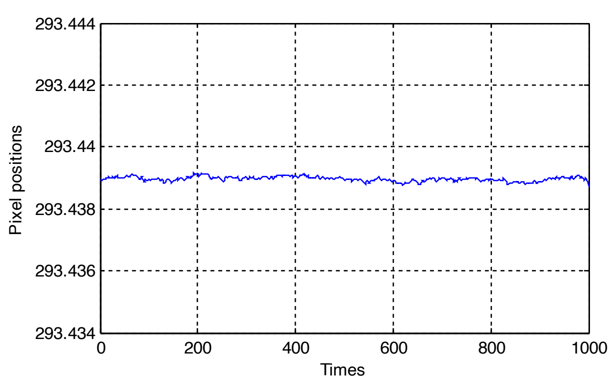

(c) Location curve after 9-th order denoising

Fig. 10. (a) Positioning wave curve Fig. 10 (b) Location result of multi-line fusion Fig. 10 (c) Location curve after 9-th order denoising.

the error value once every 10 *mm* interval, and record 26 error values in the range of 0 ~ 250 *mm*. The error data obtained are shown in Table 3.

The standard deviation of measurement error for each position is given in the Table 3. We measure the repeatability error by the mean of all standard deviations, which is 0.51 μ*m*.

5.6. Accuracy test

To verify the accuracy of our test equipment, we use the mean value of error data in Table 4 to measure the measurement accuracy. The error of the device is shown in Table.4, the error curve is shown in Fig. 13(a) .

Since the calibration grating is not parallel to the moving direction of the guide rail, the error in Fig. 13(a) contains a systematic error (cosine error). The systematic error is shown in Fig. 13(b). The systematic error can be expressed as $E = 0.2206x$-1.5947 by fitting. The fitting

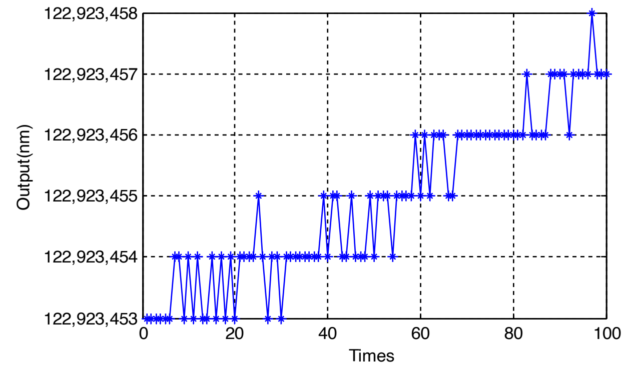

(a) Output values, slowly moving image sensor

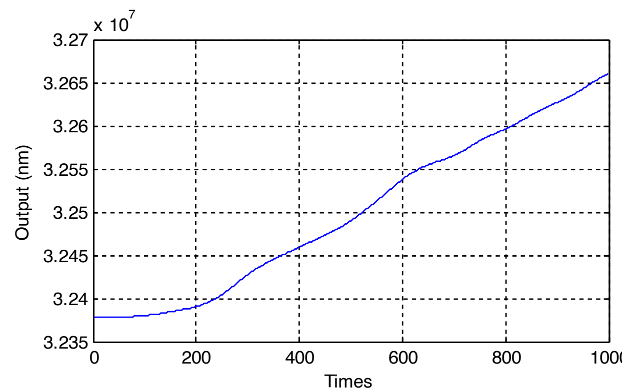

(b) Output values, faster moving image sensor

Fig. 11. (a) Output values, slowly moving image sensor Fig. 11(b) Output values, faster moving image sensor.

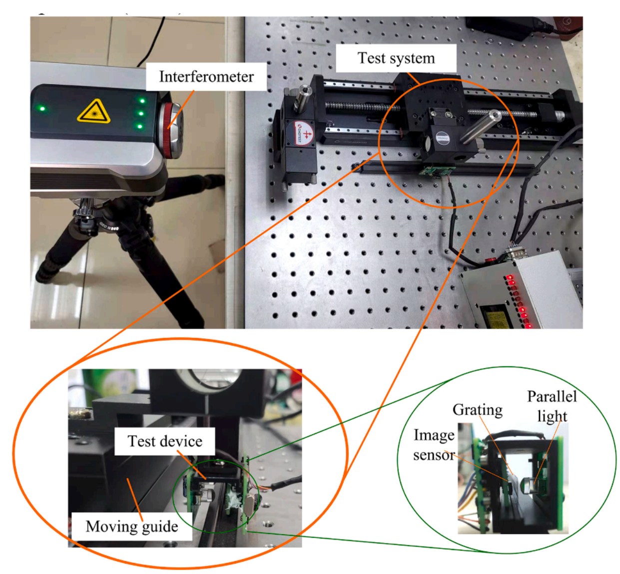

Fig. 12. Error test.

determination coefficient is $R^2 = 0.9946$.

The error curve after removing the systematic error is shown in Fig. 13(c).The mean square error is σ = 1.76 μ*m* in Fig. 13(c). We represent the precision with the numerical value of σ, so it has an accuracy of 1.76 μm, which further confirm that the proposed image-type LDM is capable of superior measurement performance.

Table 3
Repeatability test (units: *um*).

Position	No.1	No.2	No.3	No.4	No.5	standard deviation	Position	No.1	No.2	No.3	No.4	No.5	standard deviation
0	0	0	0	0	0	0.00	**130**	25.8	22.1	24.1	23.8	24.5	1.34
10	2.8	1.95	2.6	1.99	2.2	0.38	**140**	30.1	25.6	28.5	27.5	29.8	1.09
20	5.3	4.9	5.2	5.1	5.2	0.15	**150**	34.7	35.7	33.4	34.5	34.2	0.83
30	4.4	3.9	3.8	5.6	5.5	0.16	**160**	34.0	31.7	32.3	35.1	35.8	0.32
40	7.0	8.2	7.1	7.5	7.8	0.50	**170**	37.7	36.4	35.4	36.9	36.9	0.47
50	9.4	9.1	8.6	8.9	9.1	0.29	**180**	37.6	35.1	36.2	39.1	38.9	0.39
60	9.4	9.8	8.9	9.2	9.2	0.33	**190**	43.5	43.1	42.8	43.2	43.4	0.27
70	13.4	13.2	12.2	13.1	13.4	0.50	**200**	43.7	42.7	43.8	43.1	43.5	0.46
80	15.7	14.1	12.7	14.8	15.4	0.44	**210**	44.4	43.4	43.5	44.1	44.5	0.51
90	15.6	19.5	20.1	15.1	15.2	0.56	**220**	45.9	42.2	43.8	44.5	45.6	0.55
100	20.8	21.5	24.1	19.8	20.1	0.48	**230**	48.8	47.1	46.9	47.9	47.5	0.63
110	21.7	22.1	24.1	21.2	19.5	0.99	**240**	52.6	50.8	51.2	52.4	52.4	0.30
120	23.6	25.6	28.5	23.1	23.2	0.98	**250**	52.0	51.2	53.1	53.5	53.5	0.39

Table 4
Error data (units: *um*).

Position	Error	Position	Error
0	0.00	**130**	24.06
10	2.31	**140**	29.12
20	5.14	**150**	34.50
30	5.70	**160**	35.64
40	7.52	**170**	36.94
50	9.02	**180**	39.34
60	9.30	**190**	43.20
70	13.06	**200**	43.36
80	15.08	**210**	44.22
90	15.04	**220**	45.22
100	20.06	**230**	47.82
110	20.44	**240**	52.66
120	23.10	**250**	53.48

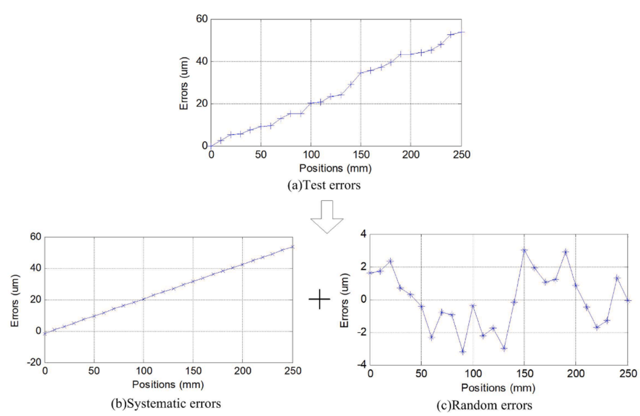

Fig. 13. Error curve.

5.7. Error analysis

Through the error test experiment, it can be seen that there are system error and random error in the measurement error. The random error has a great influence on the measurement accuracy. The analysis error is as follows:

System error. It is the cosine error caused by the angle between the calibration grating and the moving direction of the image sensor. The error can be eliminated by reducing the angle between the calibration grating and the moving direction of the image sensor.

Random error. It is the error caused by the change of the distance between the image sensor and the calibration grating. According to Fig. 3(b), the distance between the image sensor and the calibration grating should be less than 1 *mm*, and the distance should be kept constant. In our experiment, the distance between the image sensor and the calibration grating will inevitably change due to the use of the translation guide to drive the image sensor directly. If the sliding bearing and spring device are used to fix the image sensor to keep the distance constant, the random error will be greatly reduced. In addition, the factors of random error also include: 1) the size of the feature on the grating had some deviation against the ideal value. 2) the pixel size had deviation against the ideal value.

6. Conclusions

Absolute LDM via image processing algorithm outperforms traditional technology, giving it distinct advantages in the absolute high-performance displacement measurement field. In a previous study, we found that the use of an imaging lens for image magnification enhances measurement resolution, but also makes the measurement device larger, produces a more complex optical path, and makes the system vulnerable to vibration, virtual focus, and other effects. A lensless imaging LDM method was established in this study based on grating projection imaging, a coding method was developed based on the linear array image sensor, and the image processing algorithm was applied for subdivision operation.

The range of the designed LDM device was determined to be 250 *mm*; 500 sets of coding standards can be marked in the range and 500000-fold subdivision is possible. After applying the subdivision algorithm, the LDM device can achieve a measurement resolution of 1 *nm* with 1.78 μ*m* measurement accuracy (mean square deviation). The research presented in this paper may provide a sound basis for future high-resolution and high-reliability LDM technologies.

CRediT authorship contribution statement

Hai Yu: Data curation, Formal analysis, Funding acquisition, Methodology, Software, Validation, Writing - original draft. **Qiuhua Wan:** Conceptualization, Investigation, Project administration, Resources, Supervision. **Zhiya Mu:** Formal analysis, Visualization, Data curation. **Yingcai Du:** Writing - review & editing. **Lihui Liang:** Writing - review & editing.

Funding

This project is supported by the National Natural Science Foundation of China (Grant No. 52075520 and 51605465) and Key Laboratory of Criminal Inspection in Sichuan Province (2018YB03).

Declaration of Competing Interest

The authors declare that they have no known competing financial interests or personal relationships that could have appeared to influence the work reported in this paper.

References

[1] F. Liu, W. Wang, L. Wang, et al., Error analyses and calibration methods with accelerometers for optical angle encoders in rotational inertial navigation systems, Appl. Opt. 52 (2013) 7724–7731.
[2] Z. Zhang, F. Ni, Y. Dong, et al., A novel absolute angular position sensor based on electromagnetism, Sens. Actuators A 194 (2013) 196–203.
[3] D. Zhang, S. Zhao, Q. Zheng, et al., Absolute capacitive grating displacement measuring system with both high-precision and long-range, Sens. Actuators, A 295 (2019) 11–22.
[4] M. Fu, C. Li, G. Zhu, H. Shi, F. Chen, A High Precision Time Grating Displacement Sensor Based on Temporal and Spatial Modulation of Light-Field, Sensors. 20 (3) (2020) 921.
[5] N. Cai, W. Xie, H. Peng, et al., A novel error compensation method for an absolute optical encoder based on empirical mode decomposition, Mech. Syst. Sig. Process. 88 (2017) 81–88.
[6] C. Yang, S.O. Oyadiji, Theoretical and experimental study of self-reference intensity-modulated plastic fibre optic linear array displacement sensor, Sens. Actuators, A 222 (2015) 67–79.
[7] Yu. Zhicheng, Peng Kai, Liu Xiaokang, et al., A high-precision absolute angular-displacement capacitive sensor using three-stage time-grating in conjunction with a remodulation scheme, IEEE Trans. Ind. Electron. 66 (9) (2019) 7376–7385.
[8] H. Yu, X. Jia, Q. Wan, L. Liang, C. Zhao, High-resolution angular displacement technology based on varying Moiré figure phase positions, IEEE Sens. J. 19 (6) (2019) 2126–2132.
[9] D.B. Leviton, M.S. Garza, Recent advances and applications for NASA's new, ultra-high sensitivity, absolute, optical pattern recognition encoders, Proc. of SPIE 4091 (2003) 375–384.
[10] Y. Sugiyam, Y. Matsu, H. Toyod, et al., A 3.2kHz 14-bit optical absolute rotary encoder with a CMOS profile sensor, IEEE Sens. J. 8 (8) (2008) 1430–1436.
[11] M. Tresanchez, T. Pallejà, M. Teixidó, et al., Using the image acquisition capabilities of the optical mouse sensor to build an absolute rotary encoder, Sens. Actuators, A 157 (2010) 161–167.
[12] H. Wang, J. Wang, B. Chen, et al., Absolute optical imaging position encoder, Measurement 67 (2015) 42–50.
[13] H. Yu, Q. Wan, X. Lu, et al., Small-size, high-resolution angular displacement measurement technology based on an imaging detector, Appl. Opt. 56 (3) (2017) 755–760.
[14] H. Yu, Q. Wan, X. Lu, et al., A robust sub-pixel subdivision algorithm for image-type angular displacement measurement, Opt. Laser Eng. 100 (2018) 234–238.
[15] H. Yu, Q. Wan, Y. Sun, et al., High precision angular measurement via dual imaging detectors, IEEE Sens. J. 19 (17) (2019) 7308–7312.
[16] S. Das, T.S. Sarkar, A New Method of Linear Displacement Measurement Utilizing Grayscale Image, Int. J. Electr. Electr. Eng. 1 (3) (2013) 176–181.
[17] J.S. Baji, D.Z. Stupara, B.M. Dakib, et al., An absolute rotary position sensor based on cylindrical coordinate color space transformation, Sens. Actuators, A 213 (2014) 27–34.
[18] J.A. Kim, J.W. Kim, C.S. Kang, et al., Absolute angle measurement using a phase-encoded binary graduated disk, Measurement 80 (2016) 288–293.
[19] Y. Mu, J. Jiang, N. Ding, et al., A 7.4 kHz, 20-bit image encoder with a CMOS linear image sensor, Opt. Quant. Electron. 51 (321) (2019).
[20] D.B. Leviton, B.J. Frey, Ultra-high resolution, absolute position sensors for cytostatic applications, Proc. Of SPIE 4850 (2003) 776–787.
[21] O.U. Lashmanov, A.S. Vasilev, A.V. Vasileva, et al., High-precision absolute linear encoder based on a standard calibrated scale, Measurement 123 (2018) 226–234.
[22] S. Fu, F. Cheng, T. Tjahjowidodo, M. Liu, Development of an Image Grating Sensor for Position Measurement, Sensors 19 (22) (2019) 4986.